

# The evolution of substructure II: linking dynamics to environment

Stuart P. D. Gill<sup>1</sup>, Alexander Knebe<sup>1</sup>, Brad K. Gibson<sup>1</sup>, Michael A. Dopita<sup>2</sup>

<sup>1</sup> *Centre for Astrophysics & Supercomputing, Swinburne University, Mail #31, P.O. Box 218, Hawthorn, Victoria, 3122, Australia*

<sup>2</sup> *Research School of Astronomy and Astrophysics, Australian National University, Weston Creek Post Office, ACT, 2611, Australia*

Received ...; accepted ...

## ABSTRACT

We present results from a series of high-resolution  $N$ -body simulations that focus on the formation and evolution of eight dark matter halos, each of order a million particles within the virial radius. We follow the time evolution of hundreds of satellite galaxies with unprecedented time resolution, relating their physical properties to the differing halo environmental conditions. The self-consistent cosmological framework in which our analysis was undertaken allows us to explore satellite disruption within live host potentials, a natural complement to earlier work conducted within static potentials. Our host halos were chosen to sample a variety of formation histories, ages, and triaxialities; despite their obvious differences, we find striking similarities within the associated substructure populations. Namely, all satellite orbits follow nearly the same eccentricity distribution with a correlation between eccentricity and pericentre. We also find that the destruction rate of the substructure population is nearly independent of the mass, age, and triaxiality of the host halo. There are, however, subtle differences in the velocity anisotropy of the satellite distribution. We find that the local velocity bias at all radii is greater than unity for all halos and this increases as we move closer to the halo centre, where it varies from 1.1 to 1.4. For the global velocity bias we find a small but slightly positive bias, although when we restrict the global velocity bias calculation to satellites that have had at least one orbit, the bias is essentially removed.

**Key words:** methods: n-body simulations – methods: numerical – galaxies: formation – galaxies: halos

## 1 INTRODUCTION

There is mounting evidence that the Cold Dark Matter (CDM) structure formation scenario provides the most accurate description of our Universe. Observations point towards a “standard”  $\Lambda$ CDM Universe comprised of 28% dark matter, 68% dark energy, and luminous baryonic matter (i.e. galaxies, stars, gas, and dust) at a mere 4% (cf. Spergel et al. 2003). This so-called “concordance model” induces hierarchical structure formation whereby small objects form first and subsequently merge to form progressively larger objects (White & Reese 1978; Davis et al. 1985; Tormen 1997). The outcome of such mergers, however, depends on many factors (e.g. the mass ratio of the merging halos, their relative velocities, etc.), the result of which is a varied mass accretion history for any given host system. While generally successful, the  $\Lambda$ CDM model does face several problems, one such problem being the prediction that one-to-two orders of magnitude more satellite galaxies should be orbiting their host halos than are observed

(Klypin et al. 1999; Moore et al. 1999). The lack of observational evidence for these satellites has led to the suggestion that they are completely (or almost completely) dark, with strongly suppressed star formation due to the removal of gas from the small protogalaxies by the ionising radiation from the first stars and quasars (Bullock et al. 2000; Tully et al. 2001; Somerville 2002). Others suggest that perhaps low mass satellites never formed in the predicted numbers in the first place, indicating problems with the  $\Lambda$ CDM model in general, replacing it with Warm Dark Matter instead (Knebe et al. 2002; Bode, Ostriker & Turok 2001; Colin et al. 2000). Recent results from (strong) lensing statistics suggest that the predicted excess of substructure is in fact required to reconcile some observations with theory (Dahle et al. 2003, Dalal & Kochanek 2002), although this conclusion has not been universally accepted (Sand et al. 2003; Schechter & Wambsganss 2002; Evans & Witt 2003). If, however, the lensing detection of halo substructure *is* correct and the overabundant satellite population really does exist, it is imperative to understand the

orbital evolution of these objects and their deviation from the background dark matter distribution.

The work described here focuses upon a set of numerical simulations of structure formation within the concordance model, analysing in detail the temporal and spatial properties of satellite galaxies residing within host dark matter halos. To date, typical satellite properties such as orbital parameters and mass loss under the influence of the host halo have primarily been investigated using *static* potentials for the dark matter host halo (e.g. Johnston et al. 1996; Hayashi et al. 2003). We stress that each of these studies have provided invaluable insights into the physical processes involved in satellite disruption; our goals was to augment these studies by relaxing the assumption of a static host potential, in deference to the fact that realistic dark matter halos are not necessarily axis-symmetric. Halos constantly grow in mass through slow accretion and violent mergers, possessing rather triaxial shapes (Warren et al. 1992). While a self-consistent cosmological modeling of both hosts and satellites has long been recognised as optimal, the required mass and force resolution can be difficult to accommodate (hence the use of static host potentials in most previous studies).

The first fully self-consistent simulations targeting the subject were performed by Tormen (1997) and Tormen et al. (1998). Both studies were landmark efforts, but lacked the temporal, spatial, and mass resolution necessary to explore a wide range of environmental effects. Unable to follow the satellite distribution within the host’s virial radius, satellites were instead tracked only up to and including the point of “accretion”. This allowed an analysis of the infall pattern, rather than the orbital evolution of the satellites. Ghigna et al. (1998) also investigated the dynamics of satellite galaxies in live dark matter host halos. Although greatly increasing the mass and spatial resolution, they still lacked the temporal resolution to explicitly track the satellite orbits. Instead, the orbits were approximated using a spherical static potential. More recently, Taffoni et al. (2003) used  $N$ -body simulations coupled with semi-analytical tools to explore the evolution of dark matter satellites inside more massive halos. However, they focus their efforts on the interplay between dynamical friction and tidal mass loss in determining the final fate of the satellites. Kravtsov et al. (2004) also mainly concentrate on the mass loss history of satellites using fully self-consistent cosmological  $N$ -body simulations.

In this paper we investigate the evolution of substructure and the orbital parameters of satellites using high spatial, mass, *and* temporal resolution. As outlined in Paper I (Gill, Knebe & Gibson 2004; hereafter GKGI), our suite of simulations has the required resolution to follow the satellites even within the very central regions of the host potential ( $\geq 5$ –10% of the virial radius) and the time resolution to resolve the satellite dynamics with excellent accuracy ( $\Delta t \approx 170$  Myrs).

The outline of the paper is as follows. Section 2 provides a description of the cosmological simulations employed. The analysis of the host halo and environment can be found in Section 3, with the satellite orbital parameters presented in Section 4. We then investigate the kinematic properties of the dark matter halos and satellites in Section 5. We finish with our summary and conclusions in Section 6.

## 2 SIMULATION DETAILS

Our analysis is based upon a suite of eight high-resolution  $N$ -body simulations generated using the publicly available adaptive mesh refinement code MLAPM (Knebe, Green & Binney 2001). MLAPM reaches high force resolution by refining all high-density regions with an automated refinement algorithm. The refinements are recursive: refined regions can also be refined, each subsequent grid level having cells that are half the size of the cells in the previous level. This creates a hierarchy of refinement meshes of different resolutions covering regions of interest. The refinement is done cell-by-cell (individual cells can be refined or de-refined) and meshes are not constrained to have a rectangular (or any other) shape. The criterion for (de-)refining a cell is simply the number of particles within that cell. A detailed study of the appropriate choice for this number as well as more details about the particulars of the code can be found in Knebe et al. (2001).

The force resolution is determined by the finest refinement level reached and corresponds to  $\approx 2h^{-1}$  kpc for the simulations presented here. The mass of an individual low-mass particle is  $m_p = 1.6 \times 10^8 h^{-1} M_\odot$  and the halos are resolved with on the order of millions of these particles. In order to investigate the evolution of satellite galaxies and their debris high temporal sampling of the outputs was necessary. From  $z = 2.5$  to  $z = 0.5$  we have 17 equally spaced outputs with  $\Delta t \approx 0.35$  Gyrs. From  $z = 0.5$  to  $z = 0$  we have 30 outputs spaced at  $\Delta t \approx 0.17$  Gyrs. For further details please refer to GKGI.

For each of our 376 outputs the satellite galaxies were initially located using MLAPM-Halo-Finder (MHF) (GKGI). This provided us with a list of all satellites and their internal properties at each individual redshift under consideration. However, as we are more interested in orbital information we performed a detailed time analysis of those satellites that were within two times the virial radius of the host halo at its formation time (using MLAPM-Halo-Tracker: MHT). For a detailed description of the halo finders and their effectiveness we refer the reader to GKGI.

## 3 HOST HALOS AND THEIR ENVIRONMENT

In Table 1 we summarise the relevant characteristics of the eight host halos. The derivation of these properties is detailed in Sections 3.1-3.4.

quantities presented discussed in this Section.

### 3.1 Canonical Properties

A simple MHF analysis of the simulation at redshift  $z = 0$  provides us with the relevant information for the host halo. At  $z = 0$  the halo masses range from  $1$ – $3 \times 10^{14} h^{-1} M_\odot$  where mass here was defined to be that within the virial radius  $R_{\text{vir}}$ . The virial radii in turn at which defined to be the point where the mean averaged density of the host (measured in terms of the cosmological background density  $\rho_b$ ) drops below  $\Delta_{\text{vir}} = 340$  with  $M_{\text{vir}}$  being the mass enclosed by that sphere. The formation redshift  $z_{\text{form}}$  is defined here as the redshift where the halo contains half of its present day mass (Lacey & Cole 1994). Applying this criterion to our data we find that the ages of our host halos range from

**Table 1.** Properties of the eight host dark matter halos. Distances are measured in  $h^{-1}$  Mpc, velocities in  $\text{km s}^{-1}$ , masses in  $10^{14}h^{-1} M_{\odot}$ , and the ages in Gyrs.

halo	$R_{\text{vir}}$	$V_{\text{circ}}^{\text{max}}$	$M_{\text{vir}}$	$T$	$c$	$z_{\text{form}}$	age	$N_{\text{sat}}(<R_{\text{vir}})$	$\sigma_{\Delta M/M}$	formation history	richness
# 1	1.34	1125	2.87	0.67	8.7	1.16	8.30	158	0.1045	QVQQ	4.7
# 2	1.06	894	1.42	0.87	9.6	0.96	7.55	63	0.1044	QVQQ	3.1
# 3	1.08	875	1.48	0.83	5.9	0.87	7.16	87	0.1148	QVVVQ	4.3
# 4	0.98	805	1.10	0.77	7.7	0.85	7.07	57	0.0947	VQQ	2.9
# 5	1.35	1119	2.91	0.65	6.0	0.65	6.01	175	0.1533	V	3.6
# 6	1.05	833	1.37	0.92	8.1	0.65	6.01	85	0.1544	V	3.2
# 7	1.01	800	1.21	0.89	6.6	0.43	4.52	59	0.2476	V	1.9
# 8	1.38	1041	3.08	0.90	3.7	0.30	3.42	251	0.2278	V	2.8

8.3 Gyrs to 3.4 Gyrs. In other words, while the masses of our systems are comparable, they are dynamically different. In Table 1, as in all following figures, the halos are ordered 1-8 in age.

The appropriate coordinate system to investigate the orbits of the satellite galaxies is given by the eigenvectors  $\vec{E}_{1,2,3}$  (with  $\vec{E}_1$  being the major axis) of the inertia tensor of the respective host halo. Moreover, the eigenvalues  $a > b > c$  can be used to describe the shape of the host and define its triaxiality  $T = (a^2 - b^2)/(a^2 - c^2)$  (Franx, Illingworth & Zeeuw 1991). The calculation of the inertia tensor is based upon the ‘‘core’’ region of the host as defined by the 6<sup>th</sup> refinement level in MLAPM; i.e. the boundary of this refinement level is an isodensity contour. The 6<sup>th</sup> refinement level surrounds material about 3000 times denser than  $\rho_b$ , or 9 times denser than the material at the virial radius. The density profiles of our host halos are well described - at least in the range from  $6h^{-1}$  kpc out to the virial radius - by the functional form advocated by Navarro, Frenk & White (1997) with concentration in the range  $c \approx 4 - 9$ . Therefore, a density of roughly  $9 \times \rho(R_{\text{vir}})$  corresponds to about the half-mass radius of the host.

### 3.2 Formation History

As we are interested in investigating the influence of host halo formation history and environment on the orbital and internal properties of the satellites galaxies living within its virial radius, it is important to understand how the host halos actually formed.

As indicated by Tormen (1997) the formation of dark matter halos can be characterised by two different phases: one corresponding to a rapid increase in halo mass, representative of a major merger. We refer to this phase as a violent (**V**) period. The second phase is one of relaxation in which the halo processes the merger and settles toward virial equilibrium. A halo may continue to accrete smaller halos during this phase. We refer to this phase as a quiet (**Q**) period.

The history of each halo is briefly outlined below using the simplified keys V or Q to signify violent or quiet episodes. For example, halo #1 has a history ‘‘QVQQ’’, that is, a quiet period around the time of formation  $z_{\text{form}}$  followed by a violent period of merging of about the same length and completed by quiet evolution for the remainder of the evolution, which lasts for twice as long as either of the two earlier episodes. The coding chain splits the evolution since formation up into more-or-less equal segments, but has nothing

to say about the absolute timescales, which differ widely from halo to halo. A qualitative summary of the eight halos follows:

*Halo #1 (QVQQ)*

A reasonably quiet history with no major violent encounters, save for a medium one at  $z = 0.7$ .

*Halo #2 (QVQQ)*

A generally quiet history with a medium size merger one quarter of the way through its evolution at  $z = 0.53$ , quickly settling for the rest of its formation.

*Halo #3 (QVVVQ)*

An initial short quiet period followed by a long and violent interaction that takes essentially the rest of its formation time to settle.

*Halo #4 (VQQ)*

An initially violent merger which quickly settles for the rest of its formation.

*Halo #5 (V)*

A very violent formation history with a strongly oscillating potential.

*Halo #6 (V)*

A steady, yet violent, formation history.

*Halo #7 (V)*

A formation history quite similar to that of halo #6.

*Halo #8 (V)*

A rapid formation history; constantly interacting with two other large halos. In this sense, a unique system.

While useful, such a qualitative description needs to be augmented with a quantitative one. In order to do so, we use the dispersion of the rate of relative mass change of the host halos:

$$\sigma_{\Delta M/M}^2 = \frac{1}{N_{\text{out}}} \sum_{i=2}^{N_{\text{out}}} \left( \frac{\Delta M_i}{\Delta t_i M_i} - \left\langle \frac{\Delta M}{\Delta t M} \right\rangle_i \right)^2, \quad (1)$$

where  $N_{\text{out}}$  is the number of available outputs from formation  $z_{\text{form}}$  to redshift  $z = 0$ ,  $\Delta M_i = M(z_i) - M(z_{i-1})$  the change in the mass of the host halo, and  $\Delta t_i$  the respective change in time. The mean growth rate at time  $i$

$$\left\langle \frac{\Delta M}{\Delta t M} \right\rangle_i = \frac{1}{N_i} \sum_{j=1}^{N_i} \left( \frac{\Delta M_i}{\Delta t_i M_i} \right)_j \quad (2)$$

is calculated for each individual output as the average over all halos  $N_i$  available at that time step.

A large dispersion  $\sigma_{\Delta M/M}$  now indicates a violent formation history whereas low values correspond to quiescent formation histories. As we can see in Table 1, our qualitative classification scheme is confirmed by the  $\sigma_{\Delta M/M}$  values.

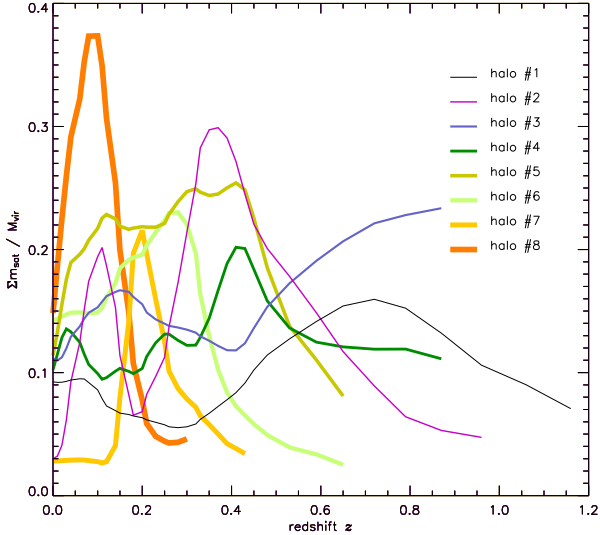


**Figure 1.** Mass locked-up in satellites within the virial radius divided by the virial mass of the host halo as a function of redshift.

### 3.3 Satellite Mass History

To gain further insight into the hierarchical build-up of the host and the evolution of its satellite population we plot the fraction of its mass locked up in the satellite distribution in Figure 1. We show the total mass of all the satellites (identified by the MHT method outlined in GKGI) living within the virial radius divided by the mass of the host halo as a function of redshift.

At  $z = 0$  the average mass of all substructure is approximately 8–9% of the host halo’s virial mass with the scatter allowing for as much as 15% and as little as 3%. We do not observe any pronounced trend for this fraction to depend on the age of the dark matter halo, which is consistent with the hierarchical model of satellite accretion: both small and large objects continuously fall in. The history is clearly reflected in Figure 1, where the infall of large satellites gives rise to the spiky nature of the curves. These large variations are, however, a combination of massive halos merging via dynamical friction and “transitory structures”. Transitory structures are small subsets of satellites that interact with a halo, but are not bound to it. An example is given in Figure 2 where we show one of these transitory events for halo #7. The peak near redshift  $z = 0.2$  for this halo in Figure 1 is caused by an object of roughly 10% of the mass of the host orbiting in the outskirts (but still within  $R_{\text{vir}}$ ) of the host halo at a relative speed of approximately  $750 \text{ km s}^{-1}$ . Figure 2 captures this event showing the host and its virial radius at redshift  $z = 0$  with the path of the satellite indicated by a line. The perturber itself is represented by its particles. Its tidal disruption while passing near the host can also be appreciated in Figure 2. We particularly highlight this galactic encounter not only to explain the rise in Figure 1 but also to raise the readers attention to the potential of already “harassed” galaxies falling into the host halo. The large peak for halo #8 in Figure 1 is due to an interaction with one of the other two large objects in the system. The violent history of halos #5 and #6 can also be seen in Figure 1. The more quiescent halos also stand out in

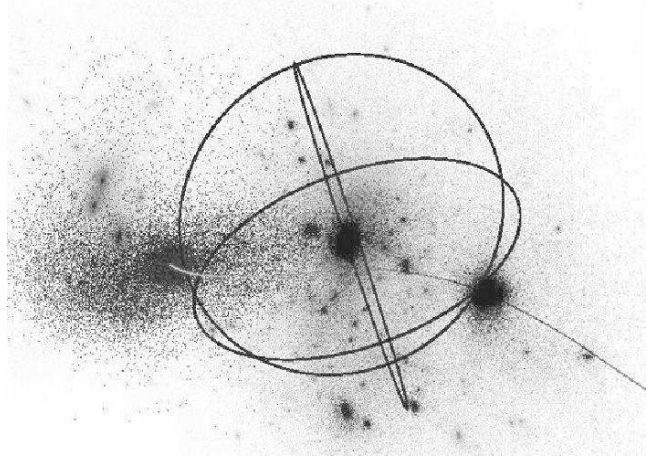


**Figure 2.** This figure shows a satellite of mass 10% the host halo that is responsible for the jump in the host’s mass accretion history. The host halo (halo # 7) is plotted as a line of sight density projection using every  $3^{\text{rd}}$  particle, whereas the satellite is represented by all its particles without a density map. The satellite enters the halo at  $z = 0.25$  (lower right) and leaves again around  $z = 0$  with the thin line indicating its orbit. The sphere shows the virial radius of the halo at  $z = 0$  and the relative velocities of the two objects is  $750 \text{ km s}^{-1}$ .

this figure, with less variation in the substructure evolution except for halo #2 with a 15% mass merger at  $z = 0.53$ .

In summary, we have selected a sample of halos displaying widely different formation histories, which should aid in gaining insight into the environmental effects of halo formation.

### 3.4 The Supply of Satellites

We now investigate the temporal evolution of satellite accretion and tidal disruption as a function of host halo environment and richness.

In Figure 3 we display the normalised number of satellites within the respective host halo as a function of time after the initial formation epoch. As we intend to measure “supply rates” rather than absolute numbers of infalling satellites we normalise the curves by the number of satellites present at the formation time of the host halo. The thin line represents the total normalised number of satellites which have been accreted, while the thick line refers to the number of *surviving* satellites. The criterion used to define tidal disruption is the reduction in the number of particles within a given satellite’s tidal radius to fewer than 15. This definition is somewhat arbitrary, although ultimately based upon the numerical resolution. For a more detailed discussion please refer to GKGI.

The increase in the total number of satellites (thin curve) reflects the “richness” of the environment around the halo: halos with a steep slope benefit from a constant supply of satellite galaxies whereas hosts that only show a mild increase draw upon a pool of fewer satellites in their immediate vicinity. This is illustrated by the case of halo #1 which lies in a particularly rich environment in which several filaments intersect (cf. Figure 4 below). As a consequence, it accretes a total of nearly five times the initial number of

satellites while simultaneously showing a high satellite disruption rate. The case of halo #3 is similar, but less extreme. Halos #7 and #8, by contrast, experience only moderate infall, and in these halos nearly all the satellites survive. The situation is illustrated for halos #1 and #8 in Figure 4, which shows the orbital paths followed by all the satellites from the formation epoch up to the present day. In the upper panel we clearly see the filament arms that feed halo #1 and how the satellites spiral into the dark matter halo. The filaments are helical because they consist of smaller satellites orbiting a larger host that is falling into the massive host halo. The small but rapid rise in the satellite infall for halo #1 (Figure 3) is caused by a group of satellites falling into the halo for the first time. In the bottom panel of Figure 4 we feature halo #8; in contrast to halo #1, halo #8 was formed in a relatively isolated region which saw a rapid collapse. We can, however, confirm that even though the satellite accretion rate in halo #8 is far less the mass of the infalling objects is much higher. This is derived from the fact that halo #8 acquires half its mass by digesting those few satellites in a time span of approximately 3 Gyrs (cf. Figure 1). We note though that there also exists a significant age difference between halo #1 and #8; this explains why halo #8 satellites are traced for a shorter time leading to the “shorter” lines in Figure 4. However, there still exist noticeable differences in the satellite accretion curves for halos #1 and #8 (cf. Figure 3) when restricting halo #1 to the first 3.5 Gyrs of its existence.

We define the substructure “richness” as the ratio of the final to initial number of satellites, and list its value for each of the eight halos in Table 1.

The number of surviving satellites is not directly correlated with the richness, but rather to the orbital characteristics of the accreted satellites, as we will demonstrate in detail below. In general, the accreted satellites are not immediately disrupted, but are progressively destroyed over time.

To further investigate the link between satellite disruption and satellite infall we calculate the ratio of disrupted (or “dead”) satellites to the total number of satellites that fall into the host halo. The result is presented in Figure 5. It is now possible to interpret the slope of this figure as the “rate of disruption” of satellite galaxies. For all halos this disruption rate (i.e. slope) is very similar. There seems to be no strongly pronounced correlation with either mass, environment or age. In this respect, the destruction rate of satellite galaxies appears to be “common” in CDM halos. However, there also appears to be a (marginal) trend that host mass is related to the ability to disrupt satellites (within the limited mass range presented here). This can be seen explicitly for halos #1 and #3: #1 destroys its satellites more efficiently than #3 and is also the more massive of the two. However, these halos also have a large difference in triaxiality (refer to Table 1). Conversely, as halo #3 is comparable in mass to halo #4 with a strikingly similar satellite destruction rate. But as halo #3 and #4 are close in triaxiality, we rather suspect the disruption rate to correlate with mass than with triaxiality. However, this correlation - if in fact correct - must also have significant scatter, as the most massive halo (#8) shows the lowest destruction rate. This might be linked to the environment and supply of new satellites, respectively.

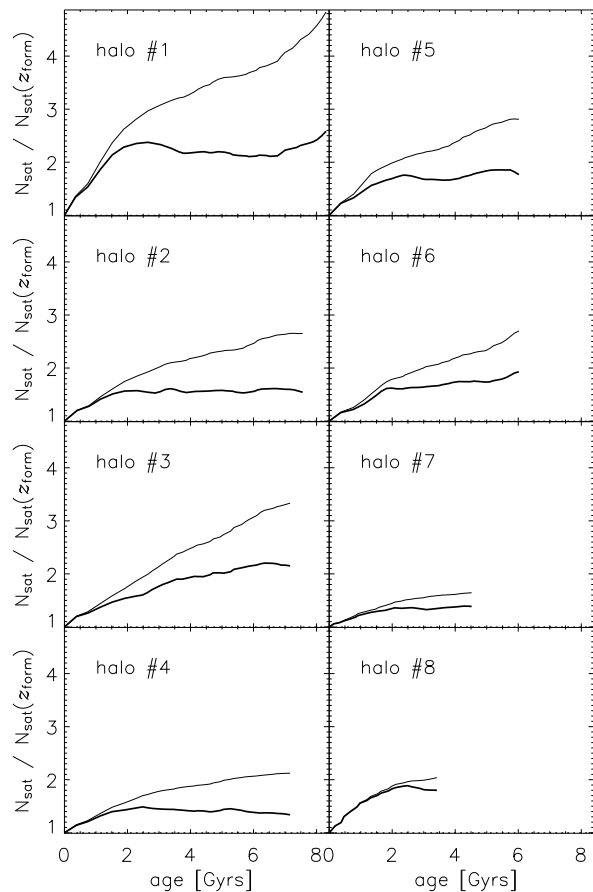


**Figure 3.** Number of satellites within the virial radius of their respective host as a function of redshift. The thin line is the total number of satellites that have fallen into the host whereas the thick line shows the number of surviving satellites. Both lines are normalised to the total number of satellites at  $z_{\text{form}}$ .

### 3.5 Summary of Host Halos and Satellite Supply

Table 1 summarises the basic properties of our halos and their environments, illustrating the variety of richness and accretion histories sampled by our simulations. The mass spectra of the satellite galaxies (although not presented) are consistent with other studies in the literature, being described by a declining power-law  $dn/dM \propto M^{-\alpha}$  with  $\alpha \approx 1.7 - 1.9$  (cf. Ghigna et al. 2000) in the range from  $2 \times 10^{10} h^{-1} M_{\odot}$  (applied mass-cut corresponding to 100 particles, which explains the rather ‘low’ number for  $N_{\text{sat}} (< R_{\text{vir}})$  in Table 1) up to  $\sim 10^{13} h^{-1} M_{\odot}$ . However, the number of satellites changes, because a) new ones are constantly being accreted (cf. thin lines in Figure 3) and b) they are being concurrently disrupted (cf. Figure 5). We also observe that the destruction rate is nearly identical for all our host halos, making it (nearly) independent of mass, age, and triaxiality. Further, as seen in Figure 4 satellites do not fall in isotropically (Knebe et al. 2004). Instead they are accreted via large-scale filamentary structure, with some carried in by more massive satellites with their own substructure field, confirming the results from earlier lower resolution simula-

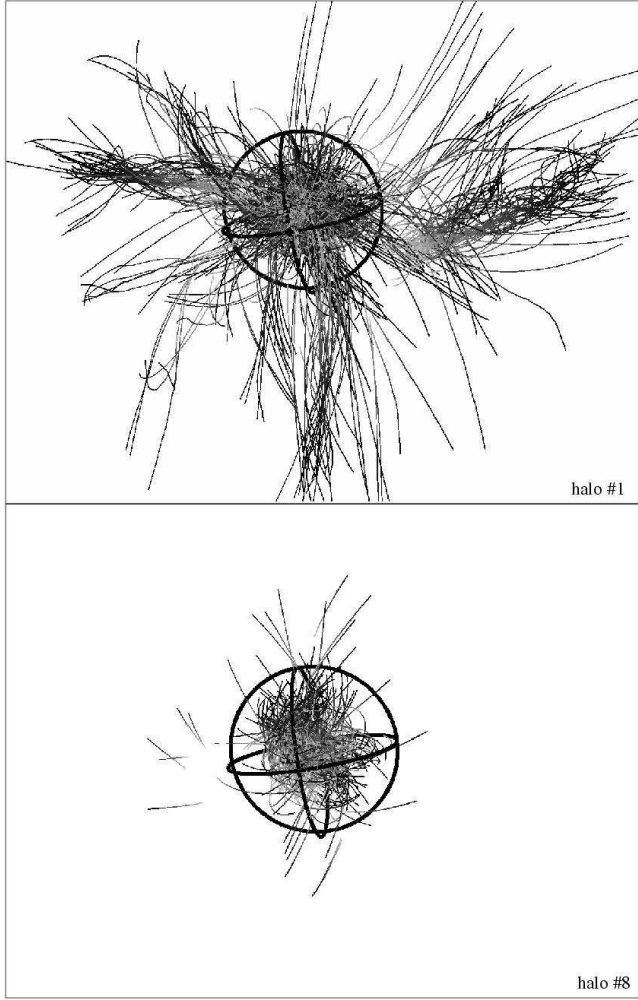


**Figure 4.** The orbits of all objects in the vicinity of the host halo are shown as lines that graduate from dark at  $z_{\text{form}}$  to light  $z = 0$ . The black spheres have a  $2h^{-1}$  Mpc radius. The top panel shows the “rich environment” of halo #1, the bottom panel the more isolated region halo #8. While satellites continually infall into halo #1, halo #8 saw an early, rapid infall of essentially all its associated satellite substructure.

tions (Hatton & Ninin 2001; Colberg et al. 1999; Tormen 1997)

#### 4 ORBITAL PARAMETER STATISTICS

Having described the differences in the host halos, we now turn to the detailed analysis of the evolution of satellite galaxies. In the following subsections we investigate their lifetimes, orbital parameters, and derive relevant correlations and relations.

##### 4.1 Number of Satellite Orbits

In Figure 6 we show the distribution of the number of orbits for both surviving satellites (thick lines) and disrupted satellites (thin lines) at redshift  $z = 0$ . For the determination and definition of the number of orbits refer to GKGI.

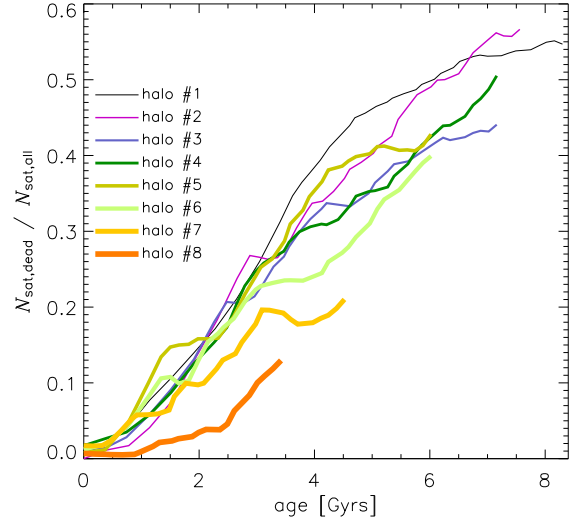


**Figure 5.** The ratio of “disrupted” satellites to the total number of satellites for satellites within the virial radius of their respective host, as a function of time, where zero age is the formation time of the halo.

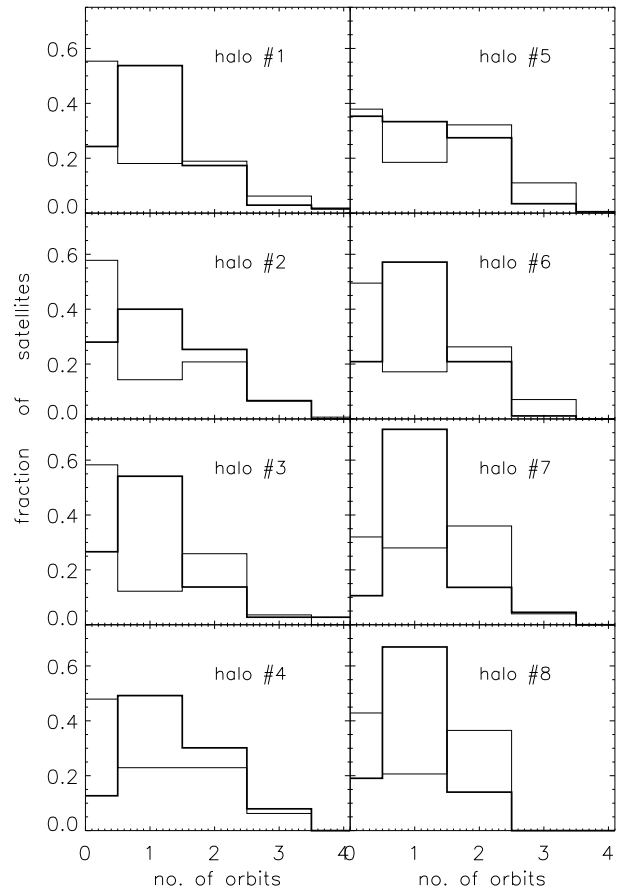


**Figure 6.** The thick histograms show the distribution of the number of orbits for all satellites that survive until redshift  $z = 0$ . The thin histograms show the distribution for disrupted satellites.

For the satellites that survived until  $z = 0$  the distribution peaks at or near one orbit for each of the eight host halos. More than 70% of the satellites have had at least one full orbit with some having as many as four, therefore making a study of the satellite dynamics valid. The length of the tail to the right of the peak at one orbit is somewhat correlated with the age of the dark matter halo. Further, the peak is more pronounced in the younger halos. However, halos #1 and #3 both show distinctive peaks at one orbit which relates to the richness of environment given in Table 1, rather than the age, as satellites are continuously falling in.

The interpretation of the distribution for the disrupted satellites is more interesting. We note that these orbits are determined by mass-less tracer particles placed at the last credible centre of the satellite before disruption. For our definition of “disruption” please refer to GKGI. The distributions are generally “flatter” with the most prominent peak near zero orbits. One explanation for such a distribution is that the infalling satellites are being disrupted before completing one orbit. This suggests that satellites contributing to this bin in the distribution are very massive and rapidly decay via dynamical friction. Having said that, we emphasize that this interpretation may be somewhat simplistic. All satellites were identified at  $z_{\text{form}}$  and we do not have an indication as to how long the satellites had already existed within the host’s progenitor. Therefore, (massive) satellites that had already been orbiting within the progenitor would be the first to be disrupted, giving this biased result. Another small contribution to this bin is from the sub-substructure. As seen in Figure 4 the systems of sub-structure are spiraling into the dark matter halo, thus the sub-structure is being destroyed in its very own (sub-)host before completing a full orbit. Regardless of this “zero orbit” peak, most of the disrupted satellites complete at least the same number of orbits as the ones which survive to  $z = 0$ .

## 4.2 Orbital Eccentricity and Pericentres

As outlined in GKGI, we define eccentricity as

$$e = 1 - \frac{p}{a}, \quad (3)$$

where the pericentre  $p$  and apocentre  $a$  distances were those last measured in the satellite’s (or the tracer particle’s) orbit. Using this definition we show in Figure 7 the distribution of the orbital eccentricity  $e$  for both live (thick lines) and disrupted satellites (thin lines). Further, we fit a Gaussian

$$P(e) = \frac{1}{\sqrt{2\pi\sigma^2}} e^{-\frac{(e-e_0)^2}{2\sigma^2}} \quad (4)$$

to the distributions (solid curves for live and dashed lines for disrupted satellites). From this fit the peak orbital eccentricity for the eight halos has an average of  $\langle e_0 \rangle = 0.61$  with an average standard deviation of  $\langle \sigma \rangle = 0.19$ . We do not observe again any correlation of peak position and width of the distribution with environment, age, host history or richness, even though  $\sigma$  appears to be larger for the younger dark matter halos. It is interesting to note that if we stack the data from the eight halos together and then separate the satellite population into differing mass bins we see little variation. This common behaviour still holds and probably

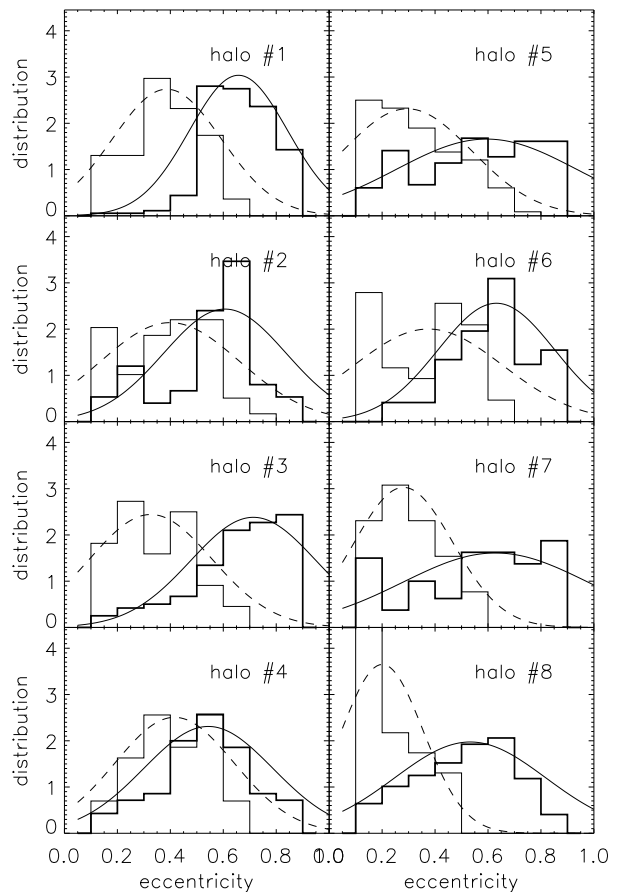


**Figure 7.** The orbital eccentricity distribution function presented as histograms for all satellites that survived until redshift  $z = 0$  (thick lines) and those which were destroyed (thin lines). The curves represent best-fit Gaussians to the distributions.

reflects the scale free force of gravity and hierarchical construction. The disrupted satellites, however, have a different distribution, almost mirroring the survivors about the  $e = 0.5$ -axis, with the peak eccentricity near  $\langle e_0^d \rangle = 0.34$  and a dispersion of  $\langle \sigma^d \rangle = 0.16$ . Thus, the destroyed satellites were preferentially on more circular orbits.

The pericentre distributions provide additional insight into the nature of the orbits of the disrupted satellites. The result for redshift  $z = 0$  can be seen in Figure 8 where  $p$  has been normalised by the virial radius of the host. Again, live satellites are represented as thick lines and disrupted ones as thin lines. A striking characteristic of these distributions is again the similarity between the halos. Moreover, we also observe a similarity in the distribution for the live and disrupted satellites. This is emphasised particularly by the best-fit Gaussians to the distributions. The maximum peak lies at 35% of the virial radius for live satellites with a mean dispersion of  $\langle \sigma \rangle = 0.12$  as opposed to 31% of  $R_{\text{vir}}$  for the disrupted ones with a dispersion of  $\langle \sigma^d \rangle = 0.11$ . Unlike eccentricity, the pericentre distribution rises quickly towards the peak and falls off moderately to the outer parts of the host halo. We already noted the lack of correlation with mass, age, environment and richness, but there is, however, a mild dependence on the state (live or dead) of the satellite

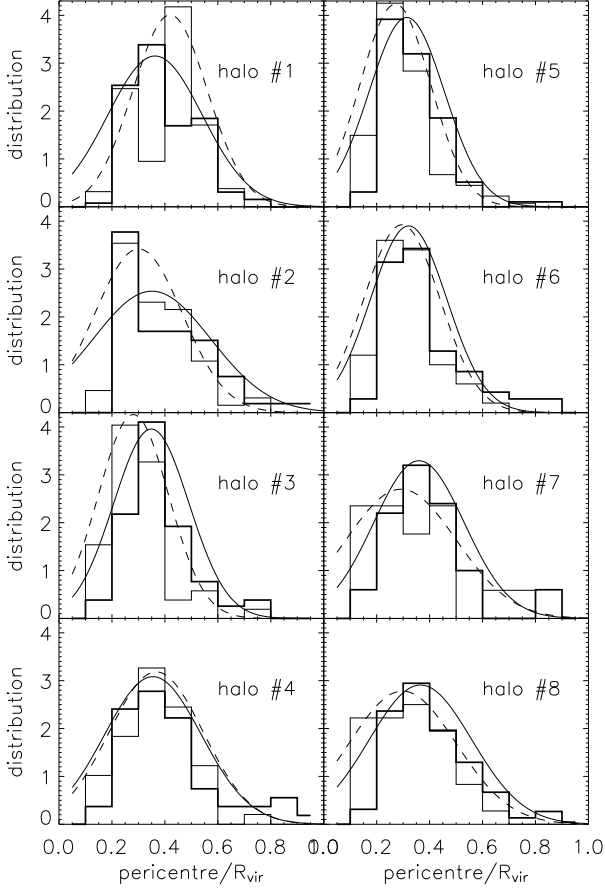


**Figure 8.** The pericentre distribution function presented as histograms for all satellites that survived until redshift  $z = 0$  (thick lines) and those which were destroyed (thin lines). The curves represent best-fit Gaussians to the distributions.

as disrupted satellites appear to have had marginally nearer excursions towards the host centre. When we stack the data from the eight halos and separate into differing satellite mass bins we again see little variation.

In summary the difference between live and disrupted satellites lies primarily in the eccentricity distribution. Disrupted satellites seem to be on more circular orbits. Since the disrupted satellites have similar pericentres to those which survive their circular nature means that they spend more time in the deeper regions of the potential well. Hence, they experience stronger tidal forces for longer periods, and are thus disrupted/dissolved more readily.

We close this subsection with an examination of the pericentre-eccentricity relation (Figure 9). The crosses represent the satellites that survived until redshift  $z = 0$ , while the diamonds represent the disrupted satellites. Although many of the features seen here are also seen in Figure 7 and Figure 8, there are two additional ones which we will comment on now.

One such feature is the bimodality in the satellite distribution of halo # 1. In this Figure there seems to be two distinct (live and dead) satellite populations orbiting within the dark matter halo. As we saw, particularly in Figure 4, this dark matter halo lies in a rich area being fed by (at

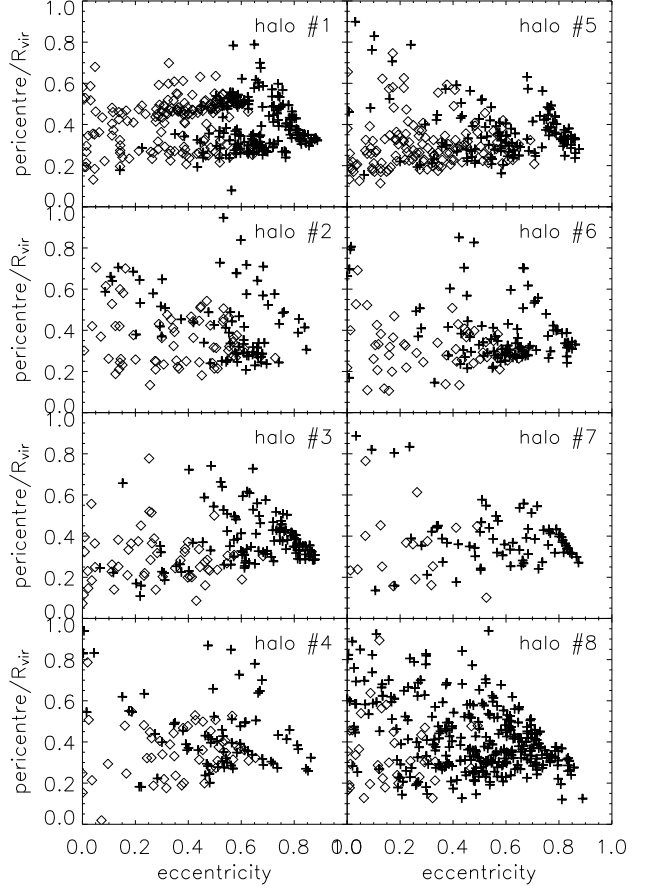


**Figure 9.** We plot the satellite eccentricity against pericentre normalised by the virial radius of the host. The crosses represent the satellites that survived until  $z = 0$  while the diamonds represent the disrupted satellites.

least) two filaments. Perhaps these two satellite populations are a remnant of the filamentary large-scale structure surrounding the host? If that is true, it is interesting that the satellites still maintain their dynamical distinctiveness after several orbits.

In addition there appears to be a distinct population of satellites with an extremely tight (anti-)correlation between eccentricities  $e \approx 0.6 - 0.9$  and pericentres  $p \approx 0.3 - 0.8$  in many halos. Upon detailed investigation these satellites were identified to have completed one orbit and were entering the halo for the first time. This is consistent with the notion of the satellites infalling on radial orbits. We investigate this point in the next section, namely the evolution of eccentricity.

### 4.3 Evolution of Eccentricity

In the previous section we considered the orbital characteristics of the satellites at redshift  $z = 0$ . We now investigate the evolution of the orbital eccentricities of the satellite family.

Figure 10 shows the eccentricity of each satellite (represented by the crosses) versus the number of orbits the satellite has completed. There is a clear trend for eccentricity to decrease as the number of orbits of a satellite increases.

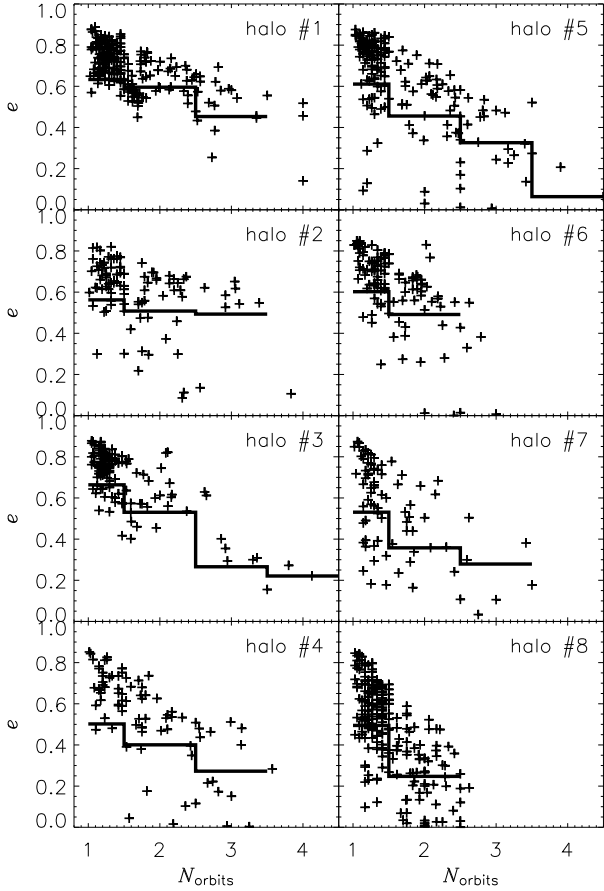


**Figure 10.** The final orbital eccentricity plotted against the number of orbits completed for each surviving satellite (crosses). The histogram shows the averaged eccentricity (see text for details).

This is also demonstrated by the histogram, which is not the “binned” results of the crosses, but is instead the average eccentricity for all satellites that had  $\geq N_{\text{orbits}}$  orbits

$$\langle e \rangle(N_{\text{orbits}}) = \frac{1}{N_{\text{sat}}(\geq N_{\text{orbits}})} \sum_{i=1}^{N_{\text{sat}}(\geq N_{\text{orbits}})} e_i(N_{\text{orbits}}). \quad (5)$$

Here,  $e_i(N_{\text{orbits}})$  is the eccentricity of satellite  $i$  after  $N_{\text{orbits}}$  orbits and  $N_{\text{sat}}(\geq N_{\text{orbits}})$  is the number of satellites with equal or more than  $N_{\text{orbits}}$  orbits.

For example, a satellite that has had 3 orbits contributes its respective value of eccentricity to the average eccentricity in the bins for 1, 2, and 3 orbits. This histogram shows a trend indicative of orbit circularisation with time. Before the work of Hashimoto et al. (2002) one would have been quick to interpret this result as dynamical friction circularising the orbits, however, they suggested otherwise. To confirm this, we selected the satellites at differing pericentre, as dynamical friction is proportional to the local density of the background field, and thus has its strongest influence at pericentre. Having done this, we saw no significant change in the above trend. Further, when we used the analytical predictions of Taffoni et al. (2003) we found that very few satellites in the population presented could be affected by dynamical friction. Therefore, we do not attribute the circu-

larising of the orbits to dynamical friction. One mechanism which could be responsible for the circularising of the orbits is the secular growth in the host halo’s mass. In response to this increase in host mass the velocity and hence the orbit of the satellite changes. Further we suggest that this change acts to circularise the orbit. Within the context of a fully self-consistent  $N$ -body simulation this claim is difficult to verify. However, in Section 5 we show that a clear relationship exists between satellite velocity dispersion and host halo mass, implying that the satellite velocities respond to a change in host mass.

Finally we compare our orbital parameters to those presented by Ghigna et al. (1998). The major difference between our respective analysis in the derivation of the orbital characteristics is that even though their host halos and satellite galaxies formed fully self-consistently in cosmological simulations they took the satellite positions and velocities and evolved them in a *static spherical potential* in order to obtain orbital characteristics. Ghigna et al. found that the satellites on radial orbits were more likely to be disrupted than those on circular orbits because they penetrate further into the dark matter halo potential well. In addition, radial orbits were quite common and circular orbits quite rare in their simulations. The average ratio of apocentre:pericentre in their outputs was 6:1, with nearly 25% of the halos on orbits with ratios in excess of 10:1. In our language this 6:1 ratio equates to an eccentricity of  $\sim 0.83$ . Hence, the Ghigna et al. satellite orbits were considerably more radial than ours. We can not reconcile this discrepancy through dynamical friction arguments. However, it could potentially be explained by the lack of a live halo. This explanation correlates with our previous finding in Section 4 for a recently infalling satellite population. This latter population constitute a distinct subpopulation with a strong (anti-)correlation in Figure 9 and an average eccentricity of  $\sim 0.8$ , quite similar to the result of Ghigna et al. .

#### 4.4 Circularity of Orbits

Another way to measure the circularity of the orbits can be written

$$\lambda = \frac{J_{\text{sat}}(E)}{J_{\text{circ}}(E)} \quad (6)$$

where  $\lambda$  is the ratio between the actual angular momentum of the satellite  $J_{\text{sat}}$  and the angular momentum of a circular orbit  $J_{\text{circ}}$  with the same energy  $E$ .

The correlation of  $\lambda$  with the the orbital eccentricity defined in Eq. (3) is presented in Figure 11 for all satellites that had at least one full orbit at redshift  $z = 0$ . The solid lines are upper limits given by the assumption that both satellite and host halo are point masses. For a derivation of this relation please refer to the Appendix.

We observe that most of the satellites follow the trend indicated by the analytical estimate showing that low-eccentricity satellites are in fact on more circular orbits. However, the trend is only suggestive but not strong with a significant scatter making it difficult to substitute one measure for the other.

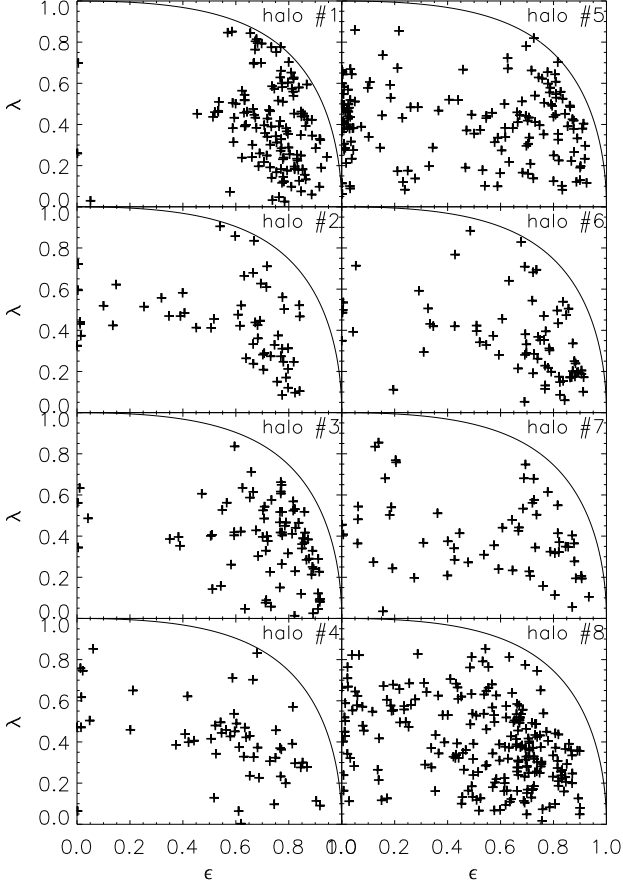


**Figure 11.** Circularity as a function of orbital eccentricity. Only satellites with at least one full orbit are considered and the solid line marks the 1:1 correlation.

## 5 DARK MATTER AND SATELLITE KINEMATICS

A controversy still exists as to whether or not cluster members trace the dark matter velocity distribution. Colin, Klypin & Kravtsov (2000) found a substantial positive velocity bias when calculating the local (or one-point) velocity bias

$$b_v(r) = \frac{\sigma_{v,\text{sat}}(r)}{\sigma_{v,\text{DM}}(r)}. \quad (7)$$

A similar yet less pronounced signal was reported by Okamoto & Habe (1999), whereas Ghigna et al. (1998) did not find any significant velocity bias in their analysis of cluster substructure. Ghigna et al. (2000) re-visited this issue, obtaining a small positive bias, but much weaker than that reported by Colin et al. (1999). Springel et al. (2001) also examined this question, suggesting a small anti-bias from their cluster simulations.

We now attempt to shed light on this controversy, by comparing the kinematical properties of the host halo and the satellite populations. We first look at the three-dimensional velocity dispersion normalised by the maximum circular velocity of the host as a function of (normalised) halo centric distance. The results for all eight host halos is presented in Figure 12. The dark matter distribution of

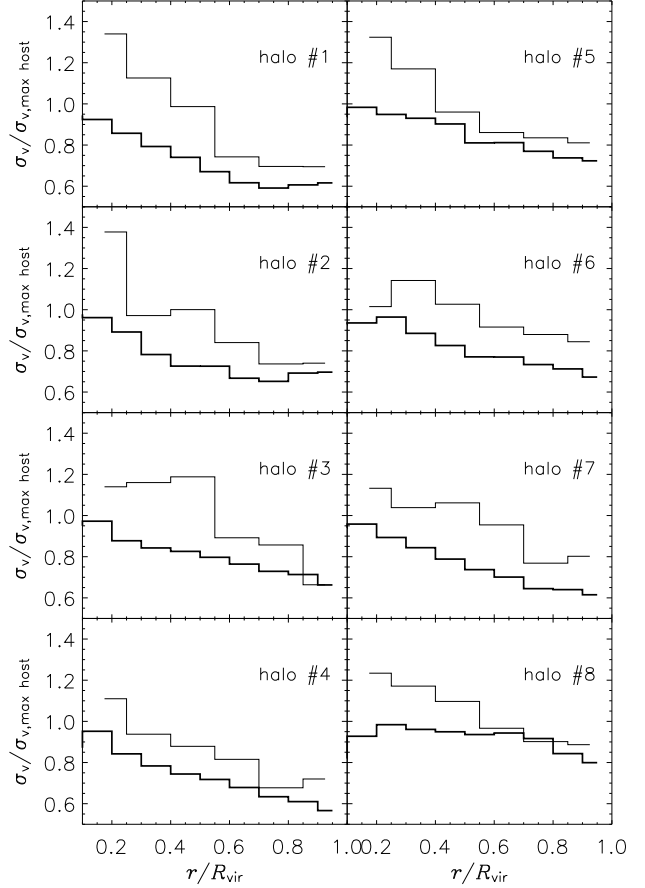


**Figure 12.** The normalised three dimensional velocity dispersion as a function of halo-centric distance normalised by the maximum circular velocity of the host halo. The dark lines represents the dark matter distribution, while the light line is the satellite distribution.

the halo is represented by the thick histograms while curves based upon the satellite galaxy population are plotted as thin histograms. Note that we do not see the characteristic “rise and fall” for the velocity dispersion of a Navarro, Frenk & White (1997) profile (cf. Lokas & Mamon 2001), because for the host halos under consideration  $\sigma_v$  peaks at about 10% of  $R_{\text{vir}}$ , which is where we start to plot the data. In general though, from the inner bin at 10% of  $R_{\text{vir}}$  out to  $R_{\text{vir}}$  we see a drop in the dark matter’s three-dimensional velocity dispersion. This drop is even more pronounced for the satellite population. Thus in general for each halo we see an increasing satellite “local velocity bias” as we get closer to the center of the host halo. In the outer regions we have  $b_v(\leq R_{\text{vir}}) \sim 1.0$  while in the inner regions  $b_v(\geq 0.1R_{\text{vir}})$  varies from 1.1 – 1.4 with the largest value for  $b_v$  being recorded for halo #2,  $b_v(\approx 0.1R_{\text{vir}}) \sim 1.4$ . Essentially for all halos though  $b_v(r) \geq 1.0$  at all radii. This result agrees with the data shown by Colin et al. (1999) and Ghigna et al. (2000), in which both groups found that the satellite population is “positively” biased with  $b_v(\approx 0.1R_{\text{vir}}) \sim 1.2 - 1.3$ . However, it contrasts with the Springel et al. (2001) findings in which a small negative velocity bias for the central regions of the cluster was claimed.

**Table 2.** The global velocity bias for the eight host dark matter halos, within the virial radius.

halo	$\sigma_{v,halo}$	$\sigma_{v,sats}$	$b_{v,global}$	$b_{v,global}^{N_{orbits} \geq 1}$
# 1	1140	1077	1.12	1.01
# 2	887	811	1.07	1.01
# 3	900	834	1.09	0.98
# 4	789	729	1.06	0.99
# 5	1170	1168	1.08	0.98
# 6	857	807	1.12	1.03
# 7	811	852	1.19	1.13
# 8	1067	1119	1.09	1.02

There is no discernible relationship between the eccentricity distribution (cf. Figure 7) and the bias seen in Figure 12; however, there is sufficient orbital distribution variation to accommodate for the variation in the bias. Improved statistics will be needed to decouple the detailed variations. However, we have shown that the velocity bias has the same basic shape for all eight halos, strengthening the case that this is a general characteristic of the satellite population.

Using all the dark matter particles and satellite galaxies within the virial radius we also calculate the global velocity bias

$$b_{v,global} = \frac{\sigma_{v,sat}(< R_{vir})}{\sigma_{v,DM}(< R_{vir})} \quad (8)$$

which is summarized for all eight halos in Table 2. It is interesting to note that we find a slight positive bias, even though Klypin et al. (1999) and Ghigna et al. (1998) both claimed that such a global velocity bias should not exist. However, Klypin et al. (1999) did hint that the possibility of a mild negative bias might exist, based upon earlier theoretical work by Carlberg (1994). Carlberg argued that as galaxies fall into the cluster for the first time they lose energy to the cluster and become systematically more bound, orbiting freely as coherent, self-gravitating units. From his simulation he measured a value of  $b_{v,global} \sim 0.8 \pm 0.1$ . From our halos we find an average global velocity bias  $\langle b_{v,global} \rangle \sim 1.103 \pm 0.002$ , which is only a very slight bias. If we restrict the global velocity bias calculation to satellites that have had at least one orbit,  $\langle b_{v,global}^{N_{orbits} \geq 1} \rangle \sim 1.019 \pm 0.002$ , a 7% decrease in the bias. The quoted errors are the scatter within the eight halos.

To further investigate the velocity bias we measure the variation from an isotropic velocity distribution using the anisotropy parameter, as seen in Figure 13

$$\beta = 1 - \sigma_t^2 / 2\sigma_r^2, \quad (9)$$

where  $\sigma_t$  measures the variance in the tangential and  $\sigma_r$  in radial direction. Once again, the dark matter ( $\beta_{DM}$ ) and satellite distribution ( $\beta_{sat}$ ) were averaged in linearly spaced radial bins, normalised by the virial radius. The dark matter distribution is represented by the thick histogram and the satellite galaxies by the thin histogram. For an isotropic distribution  $\beta = 0$ ; if  $\beta \rightarrow 1$ , then the velocities are preferentially radial; if  $\beta \rightarrow -\infty$ , they are preferentially tangential.

The standard way to represent  $\beta$  is on a logarithm scale starting from the inner percent of the virial radius. Cole & Lacey (1996) and Thomas et al. (1998) employed this technique and measured a linear increase in  $\beta_{DM}$ , starting with

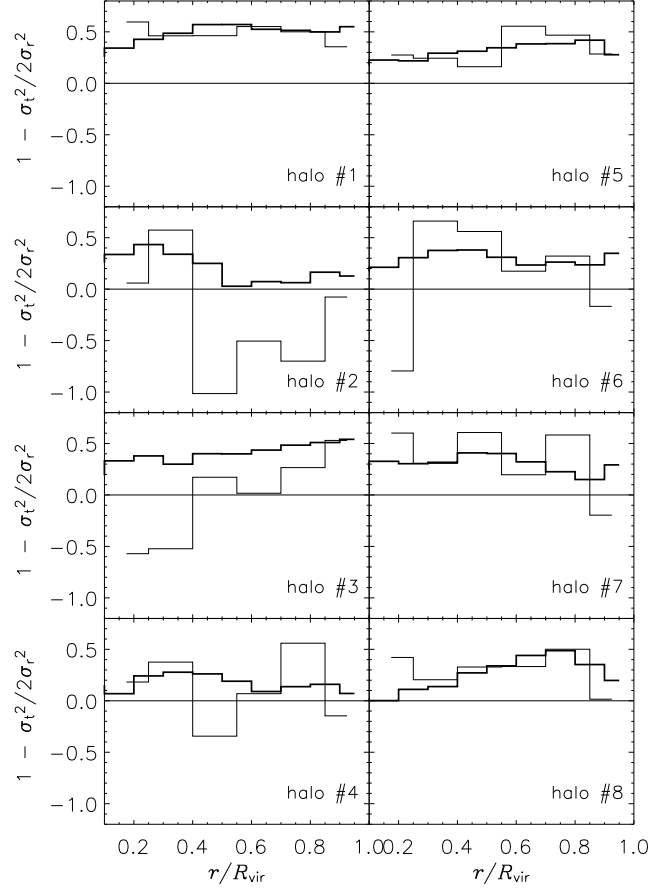


**Figure 13.** The velocity anisotropy parameter as a function of halo-centric distance. The thick line represents the dark matter distribution, while the thin line is the satellite distribution. The quantities were calculated in linear radial bins.

essentially isotropic orbits close to the halo core and becoming increasingly radial in the outer regions. In keeping with previous figures we plot the data on a linear scale. This makes it difficult to compare to this work. However, our value for  $\beta_{DM}$  does follow the same general radial relationship seen in earlier studies.

In general  $\beta_{sat}$  for the substructure population (broadly) follows the dark matter distribution. However, for halos #2 and #3, satellite orbits are generally more tangential than the dark matter background.

Finally, to gain further insight into the velocity distributions of the satellite and dark matter distributions we investigated the radial variation of the radial velocity component. Note we do not present a figure for this results. When normalised by the maximum circular velocity for all eight halos, the fraction  $v_{r,DM}/V_{circ}^{max}$  is essentially zero. Although, we do see signs of a slight dip in the outer regions. This dip is a characteristic signature of infall into the system.

## 5.1 Observational Impact

Astronomers traditionally determine the mass of galaxy cluster by assuming that the galaxy distribution is virialised.

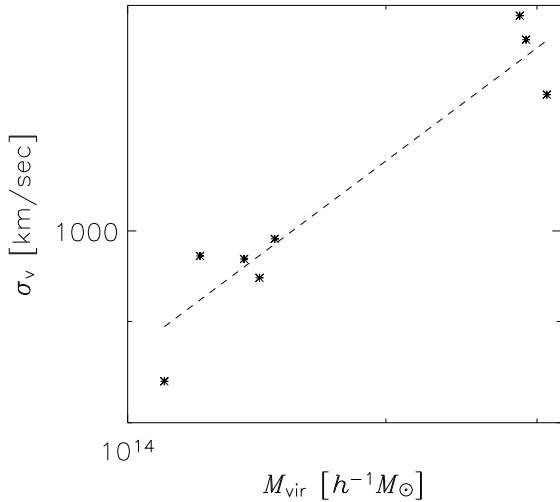


**Figure 14.** The velocity dispersion of the satellite galaxies within the virial radius of the host halo as a function of host halo mass.

The virial theorem then gives (Heisler, Tremaine & Bahcall 1985):

$$M_{\text{vir}} = \frac{R_{\text{vir}} \sigma_v^2}{G}. \quad (10)$$

In practice, however, the observational determination of the correct radius  $R_{\text{vir}}$  and velocity dispersion  $\sigma_v$  are far from straightforward, as it is difficult to determine whether or not a galaxy is a member of a cluster. Furthermore, even though we have just learned that the satellites are “stationary”, the existence of the slight global velocity bias (cf. Table 2) does impact the determination of cluster masses. Or in other words, the observed positive bias will result in an over-estimation of the halo mass when relying on the dynamics of its substructure.

From our simulations we find (to no surprise) that the velocity dispersion of a system of galaxies is a reliable indicator of the depth of the potential associated with the system. Even though we do not have a broad mass range ( $M_{\text{vir}} \sim 1 - 3 \times 10^{14} h^{-1} M_{\odot}$ ) to test this hypothesis we reconstruct the expected relationship between mass  $M_{\text{vir}}$  and velocity dispersion  $\sigma_{v,\text{sat}}$  of the satellite galaxies within the virial radius of the host halo. The results are presented in Figure 14. Each of our halos scatter about the expected analytical relationship:

$$\sigma_v \sim M_{\text{vir}}^{1/3} \quad (11)$$

This relationship can easily be understood analytically when we combine Eq. (10) and our definition for virial radius  $\Delta_{\text{vir}} \rho_b = 3M_{\text{vir}} / (4\pi R_{\text{vir}}^3)$ . The solid line displayed in the figure is the best fit power law to our eight data points. The logarithmic slope was found to be  $\sim 0.329$ , sufficiently close to the expected value of  $1/3$ .

## 6 CONCLUSIONS

If the hierarchical model of structure formation is correct then the dynamics of satellite galaxies are an important in-

redient to also understanding the formation and the evolution of galaxies. Therefore, in this paper we presented a series of self-consistent cosmological simulations of dark matter halos with the required mass and spatial resolution to follow satellite galaxies orbiting even within the central regions of the host potential. Moreover, the simulations had sufficient time resolution to actually resolve the satellite dynamics with high precision.

The first part of this study was dedicated to analysing and describing the differences in the host halos. These host halos were chosen to sample a variety of triaxialities, formation times and mass/satellite accretion, despite being of comparable mass. The halos also had very different formation histories, from quiescent to violent. When investigating the halo environment we quantified a value of “richness” which was defined to be the fraction of satellite galaxies that the halo had accreted since its formation. One interesting result from this analysis was the similar rate of satellite disruption seen for all eight halos. Furthermore, over the history of each of our halos on average about 10% of its respective mass is locked up in the satellite galaxies. Much of this mass can be attributed to massive satellites rapidly captured by dynamical friction.

But even though the eight dark matter host halos were quite different, their respective satellite population showed remarkable similarities. The average orbital eccentricity of the satellites was found to be  $e \approx 0.61$  with minimal scatter ( $\sigma \approx 0.19$ ). Moreover, the average pericentre distance of the satellites was  $p \sim 35\%$  of the virial radius for all halos, again with minimal scatter ( $\sigma \approx 0.12$ ). Satellites that were disrupted while orbiting within the host’s virial radius were replaced with a mass-less tracer particle and hence we were also able to present their orbital parameters at redshift  $z = 0$ . We found that even though they have smaller eccentricities ( $e^d \approx 0.34$ ) than the surviving ones, their pericentre distributions are nearly identical. Since the pericentres distributions of both surviving and disrupted satellites were similar, implication is that the disrupted satellites spend more time in the deeper regions of the potential well. As such, they experience stronger tidal forces for longer periods, and are thus being disrupted more readily. We also noticed that satellites with more orbits tend to have smaller eccentricities. Difficult to explain through the application of dynamical friction we attribute this to the satellite’s response to the growing host halo.

We also found that the local velocity bias at all radii is greater than one and this increases as we move closer to the halo centre. Since this is a characteristic for each of our halos, it strengthens the case that this is a general pattern of the satellite population in dark matter halos. For the global velocity bias we find an average  $\langle b_{v,\text{global}} \rangle \sim 1.103 \pm 0.002$ , a slight, but significant, positive bias. Further, if we restrict the global velocity bias calculation to satellites that have had at least one orbit we observe a 7% decrease in bias to  $\langle b_{v,\text{global}} \rangle \sim 1.021 \pm 0.002$ . Thus when we just consider the “virialised” satellites, the bias nearly vanishes. Finally we recovered the  $\sigma_v \sim M^{1/3}$  relationship between satellite velocity dispersion and halo mass.

Surprisingly, all the above stated results appear to be independent of the actual host halo and its history. We were unable to identify any trends with richness, triaxiality and/or formation time (other than the number of orbits).

Such similarities are suggestive of potential additional underlying CDM universal laws.

## 7 ACKNOWLEDGMENTS

The simulations presented in this paper were carried out on the Beowulf cluster at the Centre for Astrophysics & Supercomputing, Swinburne University. We also wish to thank Daisuke Kawata, Chris Brook, and Rob Proctor for their helpful feedback throughout the preparation of this manuscript. We acknowledge the financial support of the Australian Research Council through its Federation Fellowship (MAD) and Discovery Projects DP0208445 (MAD) and DP0343508 (BKG). MAD also acknowledges the support of the Australian National University.

The useful advice provided by the referee Fabio Governato is gratefully acknowledged, too.

## REFERENCES

- Bode, P., Ostriker, J. P., Turok, N., ApJ **539**, 93 (2001)
- Bullock, J., Kravtsov, A., Weinberg, D., ApJ **556**, 517 (2000)
- Bullock J., Kolatt T.S., Sigad Y., Somerville R.S., Kravtsov A.V., Klypin A.A., Primack J.R., Dekel A., MNRAS **559**, 321 (2001)
- Carlberg, R. G., ApJ **433**, 468 (1994)
- Colberg J.M., White S.D.M., Jenkins A., Pearce F.R., MNRAS **593**, 308 (1999)
- Coln, P., Klypin, A., Kravtsov, A., Khokhlov, A., ApJ **523**, 32 (1999)
- Coln, P., Avila-Reese, V., Valenzuela, O., ApJ **542**, 662 (2000)
- Dahle, H., Hannestad, S., Sommer-Larsen, J., ApJ **588**, 25 (2003)
- Dalal, N., Kochanek, C., ApJ **572**, 25 (2002)
- Davis, M., Efstathiou, G., Frenk, C. S., & White, S. D. M. ApJ **292**, 371 (1985)
- Evans N.W., Witt H.J., MNRAS **345**, 1351 (2003)
- Franx M., Illingworth G., de Zeeuw T., ApJ **383**, 112 (1991)
- Ghigna, S., Moore, B., Governato, F., Lake, G., Quinn, T., Stadel, J. MNRAS **300**, 146 (1998)
- Ghigna, S., Moore, B., Governato, F., Lake, G., Quinn, T., Stadel, J. MNRAS **544**, 616 (2000)
- Gill, S.P.D., Knebe, A., Gibson, B.K. 2004, MNRAS, in press
- Hashimoto, Y., Funato, Y., Makino, J., ApJ **582**, 196 (2003)
- Hatton S., Ninin S., MNRAS **576**, 322 (2001)
- Hayashi, E., Navarro, J., Taylor, J., Stadel, J., Quinn, T., ApJ **584**, 541 (2003)
- Heisler, J., Tremaine, S., Bahcall J., N., ApJ **298**, 8 (1985)
- Johnston, K., Hernquist, L., Bolte, M., ApJ **465**, 278 (1996)
- Klypin A., Gottlober, S., Kravtsov, A., Khoklov, A., ApJ **516**, 530 (1999)
- Knebe A., Green A., Binney J., MNRAS **325**, 845 (2001)
- Knebe A., Devriendt J., Mahmood A., Silk J., MNRAS **329**, 813 (2002)
- Knebe A., Gill S.P.D., Gibson B.K., Lewis G.F., Ibata R.A., Dopita M.A., ApJ **347**, 7 (2004)
- Kravtsov A.V., Gnedin O.Y., Klypin A.A., ApJ submitted, astro-ph/0401088
- Lacey, C., Cole, S., MNRAS **281**, 716 (1996)
- Lokas, L., Mamon, A., MNRAS **321**, 155 (2001)
- Moore, B., Ghigna, S., Governato, F., Lake, G., Quinn, T., Stadel, J., Tozzi, P., ApJ Lett. **524**, 19 (1999)
- Navarro J., Frenk C.S., White S.D.M., ApJ **490**, 493 (1997)
- Thomas P. A. et al. MNRAS **296**, 1061 (1998)
- Tormen, G., Bouchet, F., White, S., MNRAS **286**, 865 (1997)
- Tormen, G., MNRAS **290**, 411 (1997)
- Tormen, G., Diaferio, A., Syer, D., MNRAS **299**, 728 (1998)
- Sand, D. J., Treu, T., Smith, G. P., Ellis, R. S., astro-ph/0310703
- Schechter & Wambsganss ApJ **580**, 685 (2002)
- Somerville, R. ApJ **572**, 23 (2002)
- Spergel, D. N., Verde, L., Peiris, H. V., Komatsu, E., Nolta, M. R., Bennett, C. L., Halpern, M., Hinshaw, G., Jarosik, N., Kogut, A., Limon, M., Meyer, S. S., Page, L., Tucker, G. S., Weiland, J. L., Wollack, E., Wright, E. L., ApJ Suppl. **148**, 175 (2003)
- Springel, V., White, S., D., M., Tormen, G., Kauffmann, G., MNRAS **328**, 726 (2001)
- Taffoni G., Mayer L., Colpi M., Governato F., MNRAS **341**, 434 (2003)
- Tully, B., Somerville, R., Trentham, N., Verheijen, M., ApJ **569**, 573 (2002)
- Warren, M. S., Quinn, P. J., Salmon, J. K., Zurek, W. H., ApJ **399**, 405 (1992)
- White, S. D. M., & Rees, M. MNRAS **183**, 341 (1978)

## APPENDIX: ANALYTICAL ESTIMATE FOR CIRCULARITY PARAMETER

We wish to establish a correlation between the circularity

$$\lambda = \frac{J_{\text{sat}}(E)}{J_{\text{circ}}(E)}, \quad (12)$$

where  $J_{\text{sat}}(E)$  measures the angular momentum of an individual satellite with total energy  $E$ .  $J_{\text{circ}}(E)$  is the corresponding angular momentum for a circular orbit with the same energy  $E$ .

The connection needs to be derived using the fact that both orbits share the same total energy, so we wish to express  $E$  as a function of  $J$  in both cases, where the general expression for  $E$  and  $J$  reads:

$$E = \frac{1}{2}v^2 - \frac{GM}{r} \quad (13)$$

$$J = |\vec{r} \times \vec{v}|$$

### Circular Orbits

For a circular orbit we know that  $|\vec{r} \times \vec{v}|$  reduces to

$$J_{\text{circ}} = rv_{\text{circ}} \quad (14)$$

as both vectors are always orthogonal. Moreover, the circular velocity is given by

$$v_{\text{circ}}^2 = \frac{GM}{r} \quad (15)$$

where  $M$  is the total mass of the host halo (assumed to be a point mass).

Combining this knowledge with Eq. (13) we arrive at

$$J_{\text{circ}} = GM \frac{1}{\sqrt{-2E}} \quad (16)$$

### Keplerian Orbits

For Keplerian orbits the situation is a little more complicated. We know that the solution in spherical coordinates for closed orbits looks like

$$r = \frac{J_{\text{sat}}^2}{GM(1 - \epsilon \cos \phi)}, \quad (17)$$

where  $\epsilon$  is the measure for ellipticity of the orbit as given by

$$\epsilon = f/a \quad (18)$$

Here  $f$  is the focal length and  $a$  the major axis of the ellipse. Geometry relates  $\epsilon$  to our eccentricity  $e$  as follows

$$\epsilon = \frac{2}{2-e} . \quad (19)$$

We still need an expression for the velocity which can be derived by using the first derivative of  $\vec{r}$  with respect to time

$$\frac{d\vec{r}}{dt} = \frac{d(r\vec{e}_r(\phi))}{dt} = \dot{r}\vec{e}_r + r\dot{\phi}\vec{e}_\phi = \dot{r}\vec{e}_r + \frac{J_{\text{sat}}}{r}\vec{e}_\phi \quad (20)$$

Evaluating  $\dot{r}$  and rearranging terms gives

$$v^2 = \frac{J_{\text{sat}}^2}{r^2} \frac{1 - 2\epsilon \cos \phi + e^2}{(1 - \epsilon \cos \phi)^2} \quad (21)$$

Inserting this knowledge into Eq. (13) again leads to

$$E = \left(\frac{GM}{J_{\text{sat}}}\right)^2 \frac{\epsilon^2 - 1}{2} . \quad (22)$$

### The Relation

We now have everything necessary to write the sought-after relation between eccentricity  $\epsilon$  and circularity  $\lambda$ ; we simply need to combine Eq. (17) and Eq. (22), keeping Eq. (19) in mind:

$$\begin{aligned} \epsilon &= \frac{2}{2-e} \\ \lambda &= \sqrt{1-\epsilon^2} \end{aligned} \quad (23)$$

This relation is plotted as a solid line in Figure 11.